



## ARTICLE

# Strength capacity of prismatic specimens for masonry constructions made of concrete voussoirs

Juan Carlos Pomares Torres<sup>1</sup>  | Antonio González Sánchez<sup>1</sup> |  
 Javier Pereiro-Barceló<sup>1</sup>  | Pascual Saura Gómez<sup>2</sup> | Benjamín Torres<sup>1</sup>

<sup>1</sup>Department of Civil Engineering,  
 University of Alicante, Alicante, Spain

<sup>2</sup>Department of Architectural  
 Constructions, University of Alicante,  
 Alicante, Spain

## Correspondence

Juan Carlos Pomares Torres, Department  
 of Civil Engineering, University of  
 Alicante, PO Box 99, Alicante 03690,  
 Spain.

Email: [jc.pomares@ua.es](mailto:jc.pomares@ua.es)

## Abstract

This research shows the results of an experimental campaign of masonry specimens tested until failure. The masonry is made of special voussoirs for the construction of arches and vaults. The voussoirs were made of plain concrete. The experimental campaign focused on obtaining the flexural and the compressive strength of this type of masonry specimens. Specimens were subjected to compressive loads with different eccentricities to obtain the axial load–bending moment interaction diagrams, which indicate the strength of these pieces against eccentric compression. The ultimate purpose of this research is to foresee the behavior of structural elements, such as arches and lowered vaults with a circular directrix, built using this type of voussoirs. These structural elements aim to reintroduce anti-funicular structural elements in bridges, culvert, tunnel, floor, and roof of buildings. Constructions that solve the basic needs of the population in any country. This innovative idea on a new block geometry, designed specifically for construction of arches, allows covering distances up to 6–7 m. The use of steel is not necessary; therefore, the risk of corrosion is eliminated. Finally, a study on the use of this new masonry type on the statics of arches is assessed.

## KEYWORDS

bows, interaction diagram, vaults, voussoirs

## 1 | INTRODUCTION

The use of arches and vaults in Architecture and Civil Engineering dates to the first river civilizations of

Mesopotamia. However, the Roman Empire developed and spread this technique throughout Europe, being used with great profusion in the construction of buildings and civil works of all kinds until the beginning of the 20th century. However, in recent decades the use of structural elements such as arches or vaults in architectural construction has practically disappeared. Stone blocks or fired clay bricks have historically always been used to execute these structural elements. The use of special

Discussion on this paper must be submitted within two months of the print publication. The discussion will then be published in print, along with the authors' closure, if any, approximately nine months after the print publication.

This is an open access article under the terms of the [Creative Commons Attribution-NonCommercial-NoDerivs](https://creativecommons.org/licenses/by-nc-nd/4.0/) License, which permits use and distribution in any medium, provided the original work is properly cited, the use is non-commercial and no modifications or adaptations are made.

© 2022 The Authors. *Structural Concrete* published by John Wiley & Sons Ltd on behalf of International Federation for Structural Concrete.

voussoirs has been limited and the use of concrete in precast elements has been rare.

Several previous works on constructions based on masonry arches are cited chronologically: Manterola studied<sup>1</sup> the different types of bridges in history. He explained the design and bearing behavior of arch bridges whose fundamental invention consists of arranging the material in a certain way—the arch shape—so that the transfer of the applied loads, from their location to the supports, was carried out by producing predominant internal compression forces. The arch was divided into voussoirs of controlled size, shape, and weight. The voussoirs were more easily obtainable and manageable, arranged in a certain order to save large spans. Lahuerta's works stood out<sup>2</sup> on calculation and design of steel reinforced masonry walls and columns in buildings. The results of these calculations were presented in various tables to facilitate the proper design and construction of these masonry elements. Grimm<sup>3</sup> studied the adverse effects of empty joints on masonry performance. Unfilled joints in brick masonry weaken the walls. A method for measuring empty joints was described and poor-quality masonry works could lead to undesirable consequences. Doherty et al.<sup>4</sup> addressed the problem of evaluating the seismic strength of brick masonry walls subjected to out-of-plane bending. A simplified procedure based on a linear displacement was presented to provide that the analytical results were as representative as possible. Huerta<sup>5</sup> carried out a historical study on the design and calculation of masonry structures in which the application of limit analysis confirmed that the most restrictive condition for the project is not strength, but stability. For a structure to be stable, its structural elements must have certain dimensions that depend, fundamentally, on the geometric shape of the structure. Gilbert<sup>6</sup> examined masonry arch bridges by means of numerical models using advances in “force lines,” “rigid block” discretization and combined ground-arch interaction models. Carbonell et al.<sup>7</sup> studied the design of a reinforced concrete vault and analyzed different solutions regarding its geometric design and arrangement of the reinforcements with the help of algorithms to obtain the economic optimization. García Sanz et al.<sup>8</sup> compared, from a sustainability perspective, the environmental impact of a horizontal masonry structure using an edge vault, with respect to a reinforced concrete waffle slab, using techniques based on life cycle analysis to quantify the energy consumed in the process of manufacturing the materials and the construction of the structure. Authors concluded that the vault consumed 75% less energy in the construction process, emitted 69% less CO<sub>2</sub> into the atmosphere, had an average manufacturing cost for small spans similar to that of a conventional slab and lower when large spans were covered, generated 171%

less waste from packaging on site, although it required a greater amount and more specialized labor. Authors showed that the vaulted construction satisfies current demands in terms of sustainability, as well as that this construction technique can coexist with the technology of today's society, resulting in a product with high economic, functional, and energetic benefits. Coccia and others<sup>9</sup> analyzed masonry arch systems and vaulted structures. Small displacements of the supports, due to different causes among which the collapse of the foundation systems or the movements of the underlying structures, can lead the masonry arch to a collapse condition due to the gradual change of its geometry. The authors presented a tool, based on a kinematic approach, for calculating the magnitude of the displacements that cause the collapse of circular arches subjected to dead loads and for evaluating the corresponding force value. Trias de Bes and Casariego<sup>10</sup> designed and built a new vaulted system with bricks and reinforced concrete for a prototype house. Urruchi-Red<sup>11</sup> compared the mechanical behavior of stone bridges as a function of the vault height and the backfill. Authors also concluded that the most used directrix in bridges was the semi-circular arch. Portioli and Cascini<sup>12</sup> proposed a model of discrete elements for the static analysis of large displacements of masonry structures. In addition, small-scale experimental tests subjected to imposed settlements were carried out to validate the proposed model. Thaickavil and Thomas<sup>13</sup> studied the behavior of cracks and the evaluation of the compressive strength of masonry prisms. A mathematical model was also proposed for estimating the compressive strength of masonry prisms by performing a multiple statistical regression of the data. The force prediction with the mathematical models was in good agreement with the experimental data. Hernando García et al.<sup>14</sup> proposed a method of analysis that allows to study the history of cracks in masonry arches until their collapse. This is not only of theoretical interest because the method can be used in the analysis of some critical cases that occur in practice. When the deformations are large, the geometry of the arch is severely distorted and the stability cannot be studied with the original geometry, it is necessary to proceed step by step considering the deformed shape.

In some cases, voussoirs of special shapes or made with polyvinylchloride (PVC) or plain concrete have been used, as in the references [15–17]. Galassi and others<sup>15</sup> carried out numerical and experimental investigations to analyze the vulnerability of voussoir arches subjected to ground settlement. They employed small-scale arch models, made of PVC blocks, and subjected to a horizontal or a vertical settlement of the support. Pomares et al.<sup>16</sup> studied the advantages of the reintroduction of arches and vaults as structural elements in current architecture. They

TABLE 1 Parameters studied by authors

Parameter considered	References
Arches, bridges	Manterola (1984), <sup>1</sup> Gilbert (2007), <sup>6</sup> Carbonell et al. (2011), <sup>7</sup> Coccia et al. (2015), <sup>9</sup> Urruchi-Rojo et al. (2017), <sup>11</sup> Hernando García et al. (2018), <sup>14</sup> Galassi et al. (2018), <sup>15</sup> Pomares et al. (2018), <sup>16</sup> Abdulhameed and Said (2019), <sup>17</sup> Tempesta and Galassi (2019), <sup>20</sup> Coccia and Di Carlo (2020) <sup>21</sup>
Masonry, wall, mortar, concrete	Lahuerta (1992), <sup>2</sup> Grimm (1994), <sup>3</sup> Doherty et al. (2002), <sup>4</sup> Gilbert (2007), <sup>6</sup> Coccia et al. (2015), <sup>9</sup> Trias de Bes and Casariego (2016), <sup>10</sup> Pomares et al. (2018), <sup>16</sup> Thaickavil and Thomas (2018), <sup>13</sup> Hernando García et al. (2018), <sup>14</sup> Galassi et al. (2018), <sup>15</sup> Abdulhameed and Said (2019), <sup>17</sup> Pavlu et al. (2019), <sup>19</sup> Tempesta and Galassi (2019) <sup>20</sup>
Vault, keystone, brick	Carbonell et al. (2011), <sup>7</sup> García Sanz Calcedo et al. (2012), <sup>8</sup> Coccia et al. (2015), <sup>9</sup> Pomares et al. (2018), <sup>16</sup> Manterola (1984), <sup>1</sup> Trias de Bes and Casariego (2016), <sup>10</sup> Grimm (1994), <sup>3</sup> Doherty et al. (2002), <sup>4</sup> Coccia and Di Carlo (2020) <sup>21</sup>
Calculation, design, construction	Manterola (1984), <sup>1</sup> Lahuerta (1992), <sup>2</sup> Grimm (1994), <sup>3</sup> Doherty et al. (2002), <sup>4</sup> Huerta (2004), <sup>5</sup> Gilbert (2007), <sup>6</sup> Carbonell et al. (2011), <sup>7</sup> García Sanz Calcedo et al. (2012), <sup>8</sup> Coccia et al. (2015), <sup>9</sup> Urruchi-Rojo et al. (2017), <sup>11</sup> Portioli and Cascini (2017), <sup>12</sup> Hernando García et al. (2018), <sup>14</sup> Pomares et al. (2018), <sup>16</sup> Tempesta and Galassi (2019), <sup>20</sup> Coccia and Di Carlo (2020) <sup>21</sup>
Environmental impact, sustainability	García Sanz Calcedo et al. (2012), <sup>8</sup> Pomares et al. (2018), <sup>16</sup> Pavlu et al. (2019) <sup>19</sup>
Strength, compression	Manterola (1984), <sup>1</sup> Doherty et al. (2002), <sup>4</sup> Urruchi-Rojo et al. (2017), <sup>11</sup> Thaickavil and Thomas (2018), <sup>13</sup> Pavlu et al. (2019), <sup>19</sup> Tempesta and Galassi (2019), <sup>20</sup> Coccia and Di Carlo (2020) <sup>21</sup>
Numerical model	Gilbert (2007), <sup>6</sup> Portioli and Cascini (2017), <sup>12</sup> Thaickavil and Thomas (2018), <sup>13</sup> Galassi et al. (2018), <sup>15</sup> Tempesta and Galassi (2019), <sup>20</sup> Coccia and Di Carlo (2020) <sup>21</sup>
Experimental tests	Portioli and Cascini (2017), <sup>12</sup> Galassi et al. (2018), <sup>15</sup> Pomares et al. (2018) <sup>16</sup>

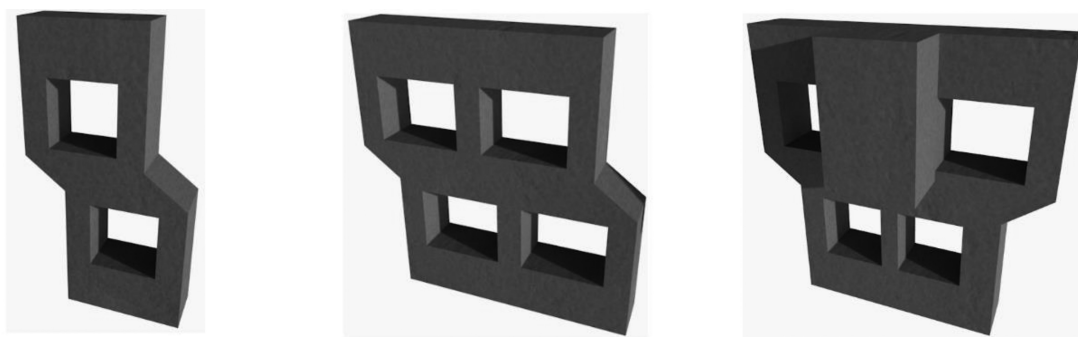
proposed a solution that did not need the addition of steel, which eliminates the risk of corrosion.<sup>18</sup> These techniques also provided an easy way to build houses in any country. This solution aimed at a more sustainable construction and was specifically designed for new buildings, although it could also be used in building retrofitting. The construction technique was simple, which few auxiliary technical and human resources for its execution, based on a traditional construction, with very low environment impact and took advantage of tradition and modern construction technology. Abdulhameed et al.<sup>17</sup> developed a new technique of concrete segments for the manufacture of masonry arches, without the need of formwork. Authors used two construction materials: concrete segments and carbon fiber reinforced polymer. Pavlu and others<sup>19</sup> studied a concrete mix containing recycled materials, considering the consumption of natural resources, as well as the mechanical and thermal properties. The concrete was intended to use in mortarless masonry wall structures. Ten concrete mixes of different types and substitution percentage of recycled masonry aggregate and recycled expanded polystyrene were prepared. The mechanical and thermal properties were investigated experimentally. Tempesta and Galassi<sup>20</sup> presented a numerical procedure for calculating the force lines in masonry arches. The two limit force lines, which corresponded to the upper and lower limits of the range, were finally used to calculate the

safety of an arch through the identification of equilibrium states and the geometric safety factor.

As previously mentioned, masonry arch systems and vaulted structures can reach the failure due to the displacements of their supports. Coccia and Di Carlo<sup>21</sup> presented a numerical tool for calculating the structure, considering the gradual changes in geometry. The analytical model was developed within the framework of the limit analysis, according to a kinematic approach, modeling the masonry as a rigid material in compression without bearing tension and avoiding sliding failures. A parametric study was carried out to understand the influence of the main geometric parameters on the arch behavior.

As a summary, Table 1 shows the most relevant parameters studied by the different authors mentioned above.

Considering all this scientific background, the objective of this research is to study the mechanical behavior of specimens made with a special type of voussoirs. These specimens will be subjected to centered compression, eccentric compression, and simple bending in order to obtain their axial load–bending moment interaction diagram and thus be able to evaluate their strength capacity under different load combinations. Subsequently, an analytical study of an arch made with these voussoirs will be carried out and the internal forces underwent by the arch will be compared with the interaction diagram experimentally obtained to



(a) Starting concrete voussoir (b) Basic concrete voussoir (c) Keystone concrete voussoir

FIGURE 1 Geometry of the voussoirs: (a) start segment, (b) basic segment, (c) key segment

evaluate its bearing capacity under the actions considered in the current design regulations.

## 2 | DESIGN OF THE CONSTRUCTION SYSTEM

### 2.1 | Geometry of the voussoirs

Concrete voussoirs are used for the construction of the basic structural elements: arches and vaults. They have been made of plain concrete. Their shape has been designed so that their weight is low and facilitate manual handling by the operators. They have great compressive strength and a “Z” design so that they can be placed in the form of successive cantilevers. Each voussoir will be supported with the previous one and will be locked with a cement mortar. In this way, minimal auxiliary support elements are required. With this system, an attempt to return to the systems of the partitioned vaults of Moya Blanco<sup>22</sup> and Guastavino<sup>23</sup> that required minimal formwork is made.

Three types of voussoirs have been designed, one with “Z” shape, which is the basic one that generates almost the entire arch or vault, another with “L” shape that is used in the starting of the arch or vault, and a “T” shape keystone to close the arch or vault. A special starting piece made of reinforced concrete can also be included in the case of using a metal tie to absorb the horizontal reactions of the arch. In Figure 1, the three types of pieces that make up the arch can be seen.

### 2.2 | Geometry of the arch or vault

The purpose for which these voussoirs have been designed and built is the realization of structural arches and vaults that can be used for the construction of roofs

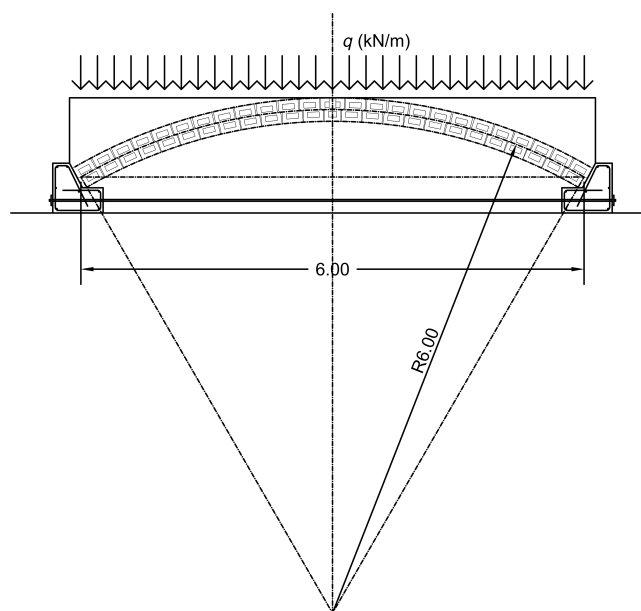


FIGURE 2 Front view of the basic geometry of the arch (dimensions in m)

in buildings and other types of low-budget constructions in safety conditions. The basic geometry of the arch or vault is indicated in Figure 2.

This type of arch can be used to cover spaces and generate roofs using a basic module like the one indicated in Figure 3.

## 3 | METHODOLOGY OF THE RESEARCH

### 3.1 | Materials: Mechanical characteristics

Conventional plain concrete poured and vibrated in wooden molds expressly made for this purpose has been

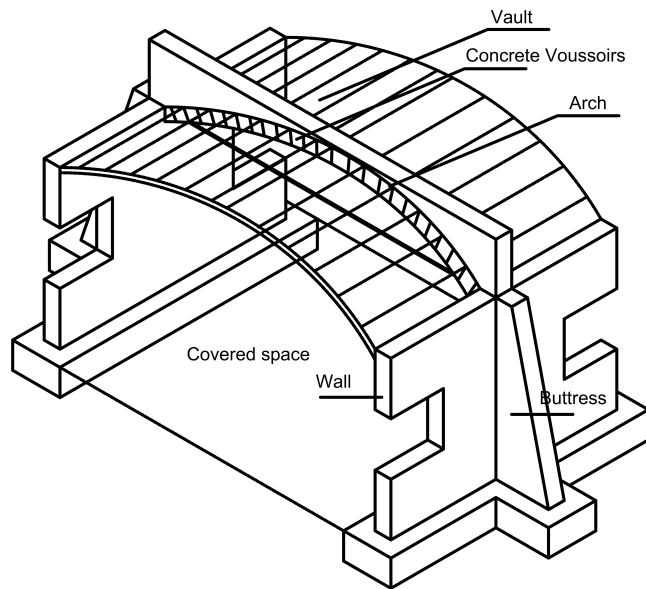


**FIGURE 3** Perspective of the basic arch module to cover a space

used for the manufacture of the three types of voussoirs. The basic dosage of the concrete was  $300 \text{ kg/m}^3$  of Portland cement with a compressive strength of 42.50 MPa, with a water-cement ratio of 0.55 and a maximum aggregate size of 20 mm. A plasticizer with a ratio of 1% of the cement weight was used to improve the workability of the concrete. The concrete compressive strength was controlled in the different mixes by means of cubic test pieces measuring 15 cm on each side, giving the average concrete compressive strength of 39.2 MPa. The coefficient of variation of the statistical values with the highest value was  $\delta = 0.0925$ , so that the dispersion of the results was very low. The concrete characteristic compressive strength was  $f_{ck} = 27.7 \text{ MPa}$  after performing the appropriate calculations and conversions according to EHE-08 design code.<sup>24</sup>

The mortar between the segments was dosed by volume with the proportions of 1:4:1, following the order of cement, sand and water. This mortar was tested under bending and compression according to the UNE-EN 1015-11 standard<sup>25</sup> with prismatic specimens of dimensions  $4 \times 4 \times 16 \text{ cm}^3$ , giving a flexural tensile strength  $f_{m,ft} = 4.91 \text{ MPa}$  and a compressive strength  $f_m = 18.48 \text{ MPa}$ . Therefore, this mortar can be classified as an M-18 according to the CTE-DB SE F<sup>26</sup> and the RC-16<sup>27</sup> standards.

### 3.2 | Preparation of the specimens

The specimens tested in the present investigation were 15 prisms, all of them with the same geometry. The specimens were made with five courses and 10 mm mortar

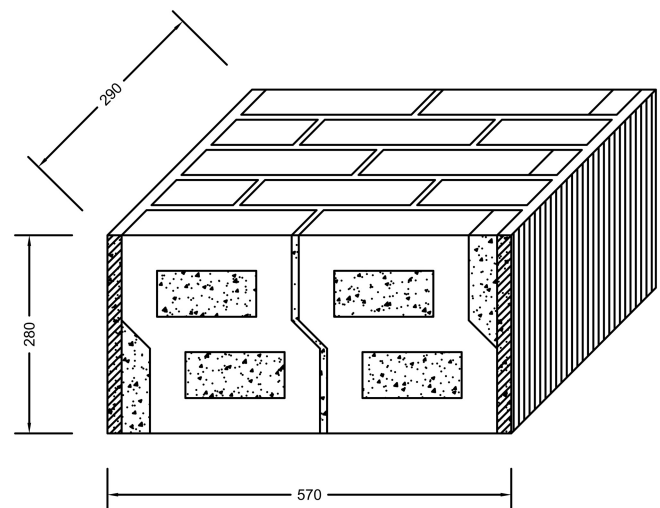


**FIGURE 4** Basic geometry of the tested specimens (dimensions in mm)

joints. The dimensions were: length  $b$  of 290 mm, the width  $t$  of 280 mm, and the height  $h$  of 570 mm. For the preparation of specimens, two basic “Z” type voussoirs were used in the three odd courses and two “L” type voussoirs plus an intermediate “Z” type were used in the two even courses. The geometry of the specimens is represented in Figure 4.

The geometric slenderness of the specimens in the direction of the test load is 1:2.03, which is a value close to 1:2 as recommended by the test standards UNE-EN 1052-1,<sup>28</sup> so that the metal plates with which the loads are applied to the faces of the specimens did not distort the results. The weight of each specimen is 85 kg.

Twelve specimens were loaded under compression with four different eccentricities  $e$  in batches of three. The eccentricities chosen were  $e_0 = 0$  (centred compression, no eccentricity),  $e_1 = t/6$  (eccentric compression, the load is applied at the limit of the central core),  $e_2 = t/4$  (eccentric compression, the load is applied in the middle half-edge), and  $e_3 = t/2.5$  (eccentric compression, the load is applied with high eccentricity, near the edge of the edge). The load was applied by means of a test frame with a 2500 kN hydraulic actuator. The control of the test was displacement control type at a speed of 0.01 mm/s. Two linear voltage displacement transducers (LVDTs) were employed. They were installed on two of specimen faces, located symmetrically with respect to the vertical directrix (Figure 5). Data was acquired by using an 8-channel acquisition card from HBM. The set-up of the test for the 12 specimens subjected to eccentric loading is shown in Figure 5, where  $e$  is the eccentricity between the axis of the load and specimen directrix.

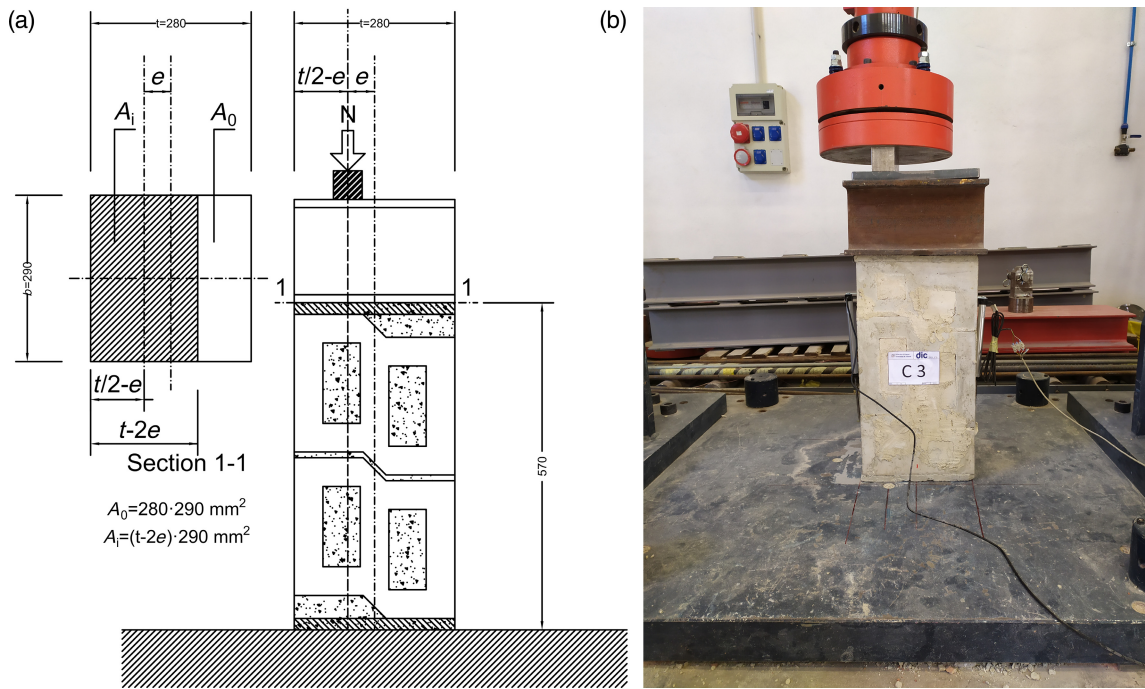


FIGURE 5 Compression test set-up: (a) eccentric compression load set-up on a standard specimen (dimensions in mm), (b) an image of the experimental test

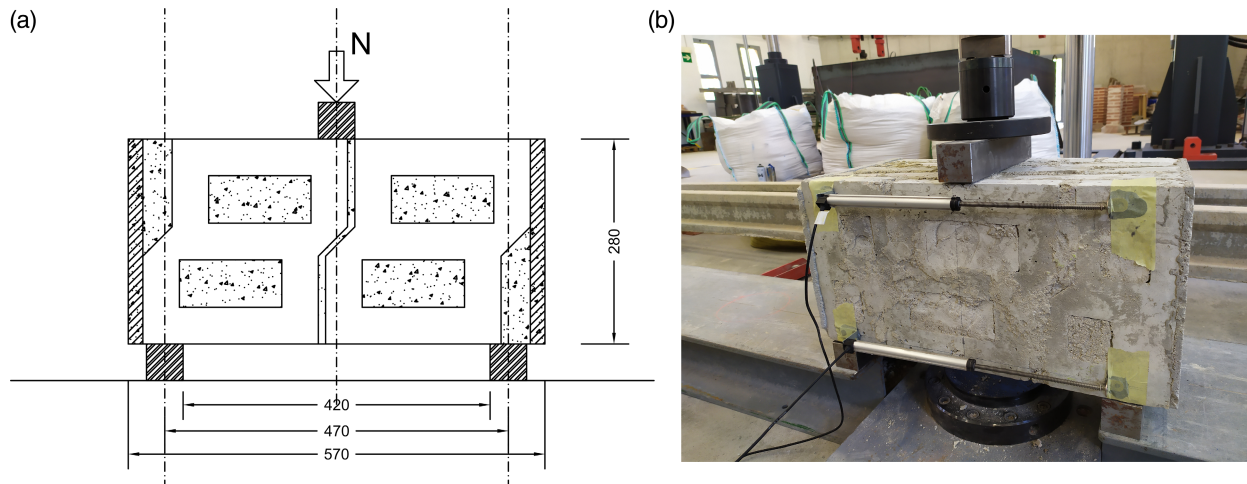


FIGURE 6 Bending test set-up: (a) simple bending load set-up on a standard specimen (dimensions in mm), (b) an image of the experimental test

Likewise, as a complement to the 12 compression tests with different eccentricities, 3 bending tests were carried out to determine the value of the flexural tensile strength. The load was applied by a 300 kN hydraulic actuator. Displacement control was used at a speed of 0.01 mm/s. The specimens were instrumented with two LVDTs installed on one of its faces, located symmetrically with respect to its horizontal directrix (Figure 6). Data acquisition was carried out using an 8-channel acquisition card from HBK. The duration of each test was between 20 and 30 min approximately.

The set-up of the test for the three specimens is reflected in Figure 6.

## 4 | EXPERIMENTAL RESULTS

### 4.1 | Strength capacity

The results of the 15 tested specimens, 12 in eccentric compression and 3 in simple bending, are shown in Tables 2 and Table 3 respectively.

TABLE 2 Summary of experimental results of compression tests

Type of load	Type of sample	Eccentricity "e" (mm)	Applied load = $N_u$ (kN)	$\sigma_{ki}$ (MPa)	$M_u$ (kN m)	$\sigma_{tk}$ (MPa)	$\sigma_{ki}/\sigma_{k0}$	$N^*$	$M^*$
Compression	E1	0	958.6		0				
	E2		869.4		0				
	E3		774.2		0				
	E Average		867.40	10.68	0	1.00	1	0	
	D1	46.666	576		26.88				
	D2		720		33.60				
	D3		638.9		29.81				
	D Average		644.97	11.91	30.10	1.12	0.744	0.991	
	C1	70	482.3		33.76				
	C2		580.9		40.66				
	C3		512		35.84				
	C Average		525.07	12.93	36.75	1.21	0.605	1.211	
	B1	112	328.6		36.80				
	B2		419.5		46.98				
	B3		388.4		43.50				
B Average	378.83		23.33	42.43	2.18	0.437	1.398		
Tensile	Extrapolation		-75		0	-0.924	-0.086	-0.086	0

Note:  $e$ , load eccentricity;  $N_u$ , ultimate axial load;  $\sigma_{ki}$ , ultimate compressive stress for eccentricity "i":  $N/A_i$ , where  $A_i$  is the area shown in Figure 5a;  $M_u$ , ultimate bending moment with respect to the center of gravity of the section,  $M_u = N_u \cdot e$ ;  $\sigma_{tk}$ , ultimate tensile stress:  $Nu/A_0$ , where  $A_0$  is the area shown in Figure 5a;  $\sigma_{k0}$ , ultimate compressive stress for eccentricity "0";  $N^*$ , ultimate nondimensional axial load:  $N^* = N_u/N_p = N_u/(b \cdot t \cdot \sigma_{k0})$ ;  $M^*$ , ultimate nondimensional bending moment:  $M^* = M_u/M_p = 8 \cdot M_u/(b \cdot t^2 \cdot \sigma_{k0})$ .

TABLE 3 Summary of experimental results of bending tests

Type of load	Type of sample	Applied load (kN)	$N_u$ (kN)	$M_u$ (kN m)	$\sigma_{xk}$ (MPa)	$\sigma_{ki}/\sigma_{k0}$	$N^*$	$M^*$
Bending	A1	69.5	0	8.17				
	A2	67.1	0	7.88				
	A3	44.9	0	5.28				
	A Average	60.5	0	7.11	1.876	0.176	0	0.234

Note:  $\sigma_{xk}$ , ultimate bending stress:  $M_u/W_y$ , where  $W_y$  is the elastic section modulus.

As can be seen in Table 2, the greater the eccentricity the greater the ultimate compressive strength of specimen  $\sigma_{ki}$  because the state of biaxial stress that the specimens undergo due to the confinement (concentrated load effect). Table 4 shows the theoretical results of the tests, not considering the effect of the concentrated load, for the compression tests. As can be seen, ultimate axial load  $N_u$  is transformed to another smaller value called  $N_u^*$  where  $N_u^* = \sigma_{k0} \cdot A_i$ . Therefore  $N_u^*$  is the ultimate axial load of specimen considering that the maximum normal stress it can bear is  $\sigma_{k0}$ , whatever the load eccentricity. This is a safety side value, which could be considered for the design. In addition, the ultimate compressive stress for each eccentricity  $\sigma_{ki}$  considering the concentrated load effect and de ratio  $\sigma_{ki}/\sigma_{k0}$  have been obtained based on Equation (1) (similar to that used for reinforced concrete). It

can be observed that these results indirectly obtained are very similar to those shown in Table 2, which were experimentally obtained.

$$\sigma_{ki} = \sigma_{k0} \cdot \sqrt{\frac{A_0}{A_i}} = \sigma_{k0} \cdot \sqrt{\frac{t \cdot b}{(\frac{t}{2} - e) \cdot 2 \cdot b}} = \sigma_{k0} \cdot \sqrt{\frac{t}{t - 2e}} \quad (1)$$

## 4.2 | Stress-deformation diagrams

The deformations of the extreme fibers of the specimens were obtained by using two LVDTs. The diagrams that relate the variation of the applied of force in each of the specimens as a function of time, and the displacements of the extreme fibers are shown in Figures 7–10.

TABLE 4 Summary of theoretical results of the factory specimens

Theoretical results								Concentrated load effect	
Type of load	Type of sample	Eccentricity "e" (mm)	$N_u^*$ (kN)	$\sigma_{k0}$ (MPa)	$M_u$ (kN m)	$N^*$	$M^*$	$\sigma_{ki}$ (MPa)	$\sigma_{ki}/\sigma_{k0}$
Compression	E	0	867.40	10.68	0	1	0	10.68	1
	D	280/6 = 46.666	578.27	10.68	26.99	0.667	0.889	13.08	1.225
	C	280/4 = 70	433.70	10.68	30.36	0.500	1.000	15.11	1.414
	B	280/2.5 = 112	173.48	10.68	19.43	0.200	0.640	23.89	2.236

FIGURE 7 Applied load and the two linear voltage displacement transducers (LVDTs) readings for the specimen E1

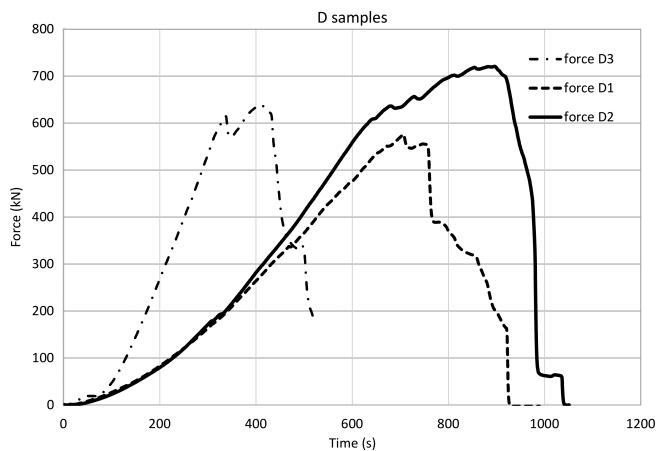
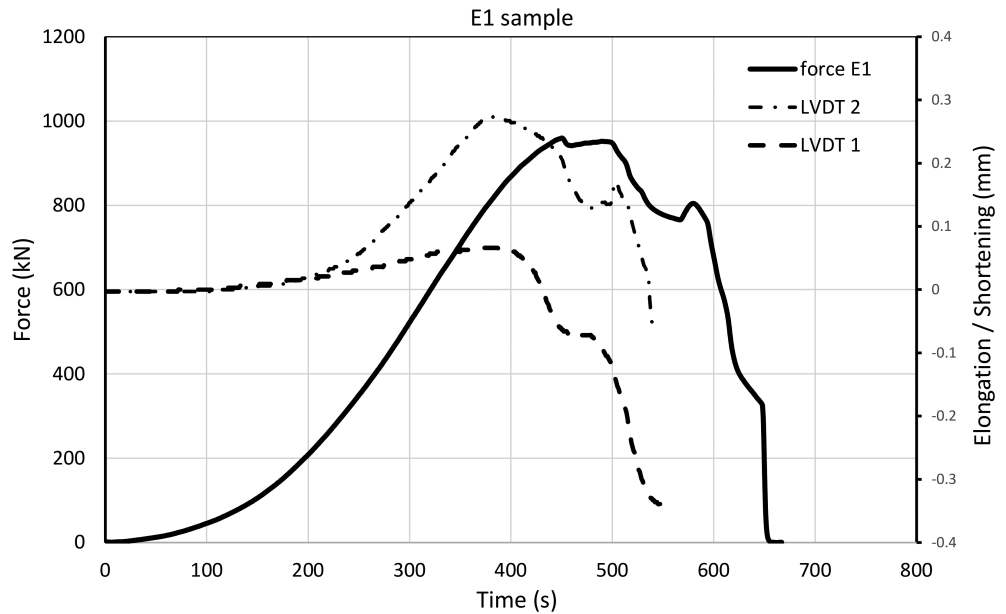


FIGURE 8 Applied forces at the specimens D

Figure 7 displays the applied force in time of the E1 specimen in which the eccentricity of the load was 0 mm (centered compression) with respect to its axis. The maximum force achieved during the test was 958.6 kN. Furthermore, the shortening and lengthening recorded by the

two LVDTs are represented in mm. In compression tests, the debonding between voussoirs and mortar took place when 70% of the maximum load was reached. At this load, LVDTs change their sign (Figures 7), that is, they began to elongate and stop shortening. The data LVDTs provided were valid up to that load value because when they began to elongate, the specimen began to fail due to another mechanism such as debonding voussoir-mortar.

Figure 8 shows applied force versus time of the specimens D in which the eccentricity  $e$  of the load is 46 mm with respect to its directrix. The highest force achieved was 720 kN in specimen 2, the lowest force was 576 kN for specimen 1, while specimen 3 achieved a force of 638.9 kN.

Figure 9 shows the applied force with respect to the shortening of the specimen C2, tested with a load eccentricity of 70 mm with respect to its directrix. The maximum recorded shortening was 0.11 mm. In addition, the test fit function has been calculated using a polynomial of degree 5.

Figure 10 shows the applied force in time of the specimens A tested under simple bending moment. The highest force achieved was 69.5 kN in specimen 1, the



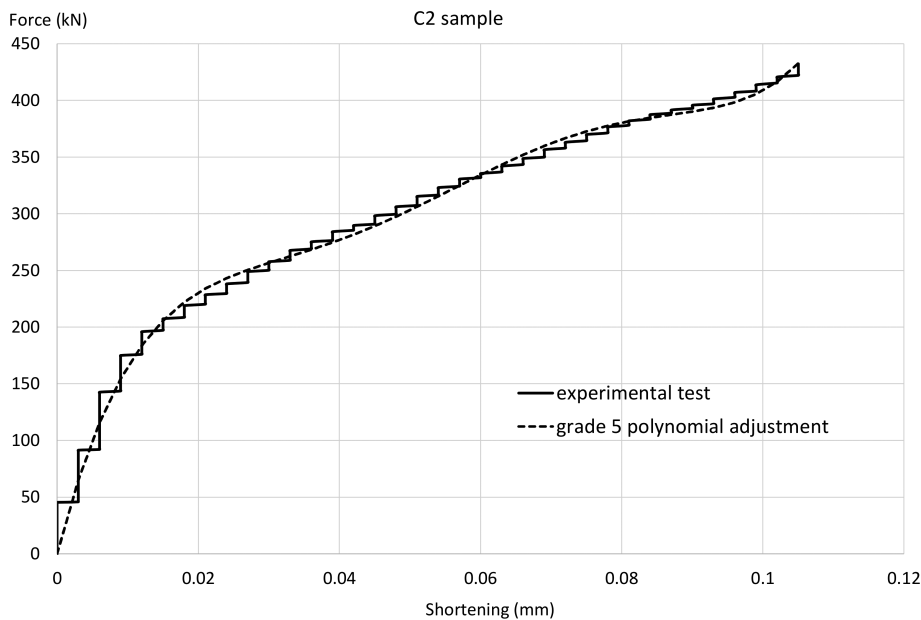


FIGURE 9 Force-shortening in eccentric compression (specimen C2)

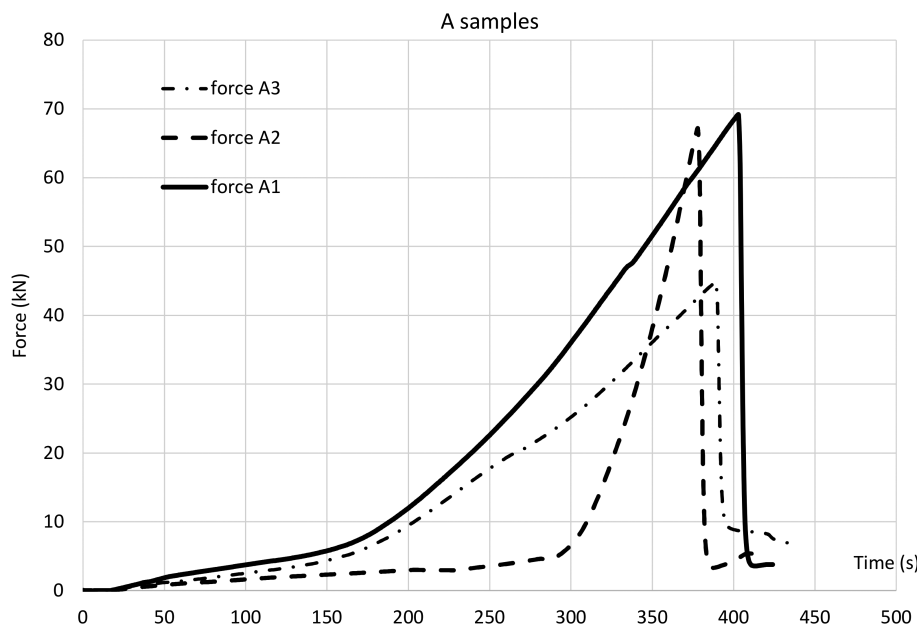


FIGURE 10 Applied force in time for type A specimens

lowest force was 44.9 kN for specimen 3, while specimen 2 achieved a force of 67.1 kN.

## 5 | INTERPRETATION AND ANALYSIS OF EXPERIMENTAL RESULTS

### 5.1 | Effect of the concentrated load

An increase in the ultimate compressive stress at specimens with eccentricity  $\sigma_{k'}$  was experimentally observed with respect to the ultimate compressive

stress at specimens with no eccentricity  $\sigma_{k0}$  due to the concentrated load effect; that varies from 1225 for small eccentricities up to 2236 for large eccentricities (Table 4). Figure 11 shows two curves that predict the increase in the ultimate compressive stress, one obtained experimentally and the other predicted by a simple mathematical model according to Equation (1), similar to that used for reinforced concrete. An increasing nonlinear behavior is observed. The theoretical curve tends to overestimate the increase in the ultimate compressive stress caused by the effect of the concentrated load but it is nevertheless capable of capturing the global trend of this phenomenon.

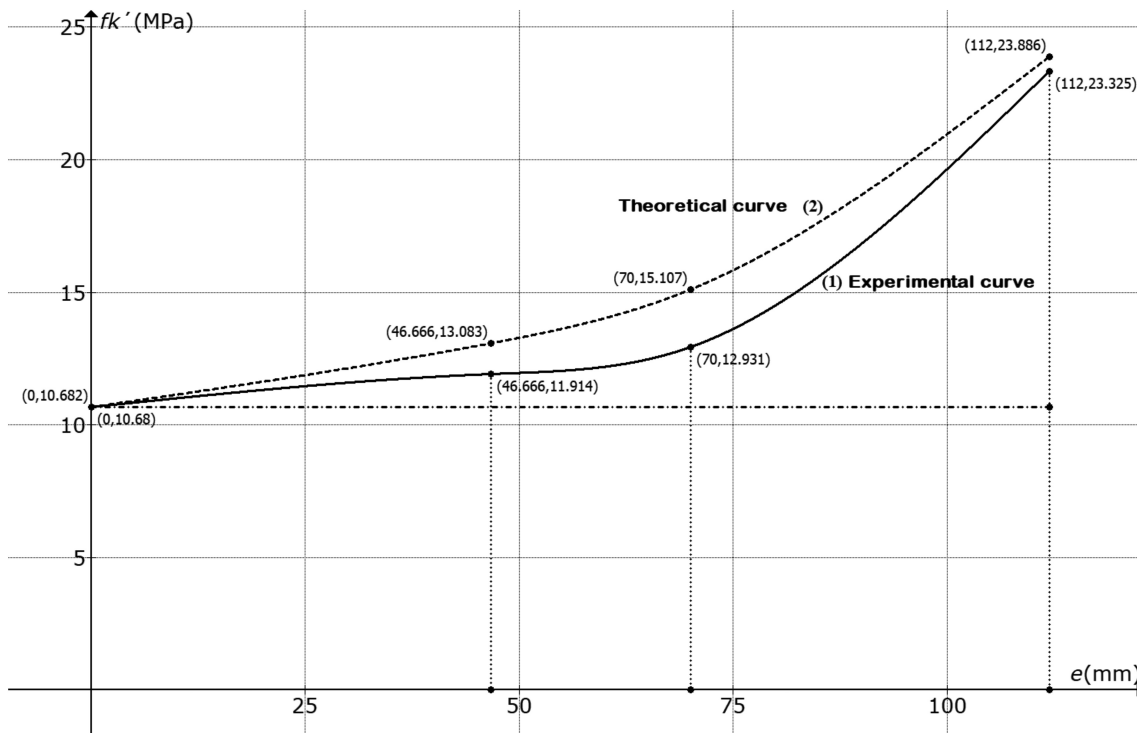


FIGURE 11 Experimental and theoretical curves to determine the ultimate compressive stress considering the concentrated load effect

## 5.2 | Axial load–bending moment interaction diagrams

The Axial load–bending moment (N–M) interaction diagrams have been elaborated with the experimental results of Section 4. Two N–M interaction diagrams have been obtained: a dimensional one (Figure 12), with the real values obtained in the tests, and a nondimensional diagram (Figure 13), dividing the axial forces by the plastic axial load  $N^* = N/(b \cdot t \cdot \sigma_{k0})$ , and the bending moments by the maximum plastic bending moment generated by the section  $M^* = 8 \cdot M/(b \cdot t^2 \cdot \sigma_{k0})$ ; where  $\sigma_{k0}$  is the real compressive strength from the factory for zero eccentricity (centered compression). Both N–M interaction diagrams include the curves obtained from the experimental values, where the concentrated load effect is appreciated, and another theoretical curve, where the concentrated load effect has not been considered.

Figure 12 shows the ultimate axial loads on the abscissa axis and the ultimate bending moments produced by the axial load eccentricity on the ordinate axis. The curves have been fitted using a polynomial of degree 3. In addition, the three values of each test (curve 1 maximum value, curve 2 mean value and curve 3 minimum value) have been represented. Likewise, the average of the experimental values curve has been drawn, which is curve 4. Curve 5 represents the theoretical N–M interaction without considering the effect of the concentrated

load. Curve 6 shows a theoretical extrapolation of the result of a pure tensile test. Curve 7 has also been drawn as a theoretical fit of the experimental results for curve 4.

Figure 13 shows the nondimensional ultimate axial loads on the abscissa axis and the nondimensional bending moments on the ordinate axis. The curves have been fitted using a polynomial of degree 3. Curve 1 shows the experimental mean values with nondimensional values. Curve 2 represents the theoretical nondimensional N–M interaction without considering the effect of the concentrated load. Curve 3 has also been drawn as a theoretical fit of the experimental results of curve 1.

This type of masonry, according to the experimental results, has an ultimate bending moment  $M_u$  under simple bending (no axial loading) with a value equal to  $0.234 \cdot M_p$ , where  $M_p$  is the plastic bending moment of the section whose value is  $M_p = (b \cdot t^2 \cdot \sigma_{k0})/8$ . This result leads to the ultimate bending strength is 17% of the ultimate compressive strength for centered compression,  $\sigma_{sk} = 0.17 \cdot \sigma_{k0}$ .

If an extrapolation of the N–M diagrams is performed, the pure tensile strength of the masonry can be computed. It is an extrapolation since the tensile strength has not been experimentally verified in this study. The result is that the tensile strength would be  $0.086 \cdot N_p$ , where  $N_p$  is the plastic axial load of the section:  $N_p = b \cdot t \cdot \sigma_{k0}$ . This implies that the masonry pure tensile strength is 8.6% of the simple compressive strength, that is,  $\sigma_{tk} = 0.086 \cdot \sigma_{k0}$ . This ratio is greater than that found in the scientific literature by other

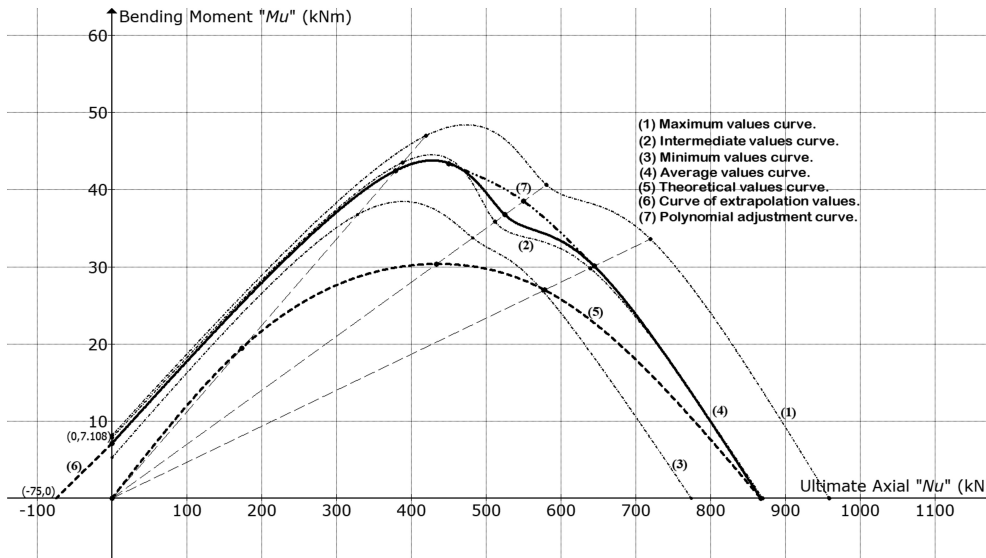


FIGURE 12 Axial load-bending moment interaction diagram (dimensional values)

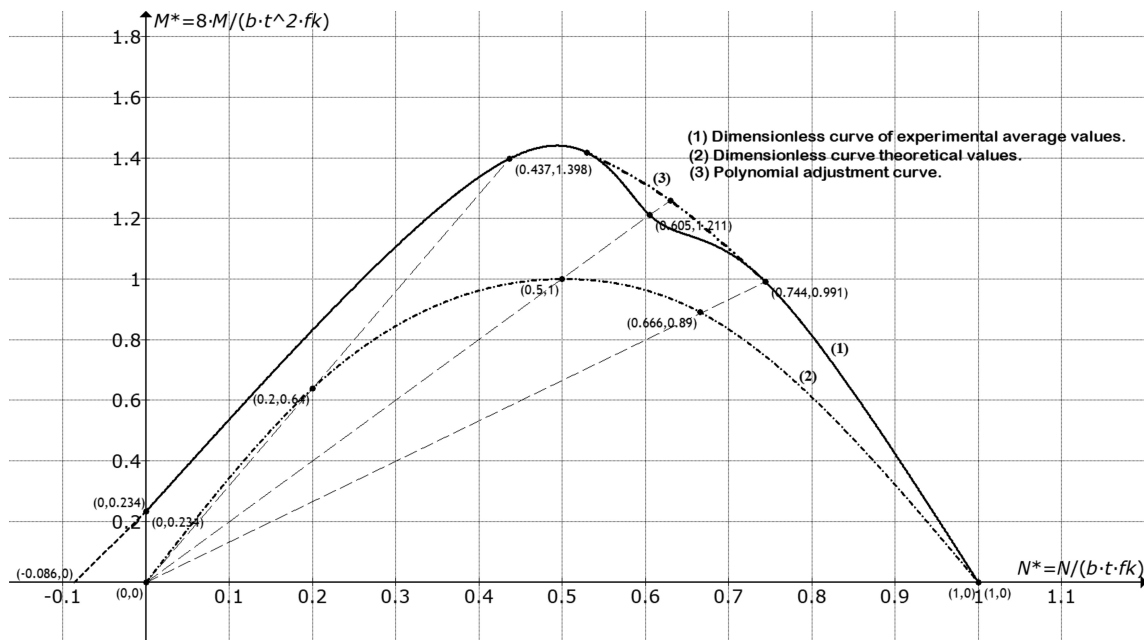


FIGURE 13 Axial load-bending moment interaction diagram (nondimensional values)

authors,<sup>29–35</sup> due to the fact that the mortar used in this experimental research had greater strength than is commonly used in masonry construction. The special geometry of the voussoirs can also influence this fact. Moreover, the qualification of the workmanship is a factor that can influence the dispersion of the masonry strength.

The ultimate compressive strength of the tested masonry with centered loading is 10.68 MPa, which is a value in accordance with other similar masonries such as concrete blocks and is an adequate value for bearing the working stress of a section of an arch or a vault. The Equation (2), proposed in the CTE-DB SE F<sup>26</sup> and the RC-16<sup>27</sup> standards, is used to analytically

predict the simple compressive strength  $f_k$  of masonry elements and its correlation with the experimental results is correct (9.179 MPa  $\approx$  10.68 MPa). The voussoirs in the structural arches normally work at compressive stresses in service between 2 and 3 MPa, for spans up to 15 m and usual loads.<sup>36</sup> This interval is of the order of 25% of the  $f_k$  obtained in Equation (2).

$$f_k = K \cdot f_b^A \cdot f_m^B = 0.55 \cdot 25^{0.65} \cdot 18^{0.25} = 9.179 \text{ MPa} \approx 10.68 \text{ MPa} \quad (2)$$

where  $k$ , nondimensional coefficient that depends on the number of holes in the prismatic element;  $f_b$ , the

compressive strength of the prismatic element;  $f_m$ , the compressive strength of the mortar.

According to the both dimensional and non-dimensional N–M interaction diagrams, the real masonry strength under both simple bending and eccentric compression, is much higher than the expected theoretical strength since the curve of the experimental results is above the theoretical curve. The reason is basically the aforementioned concentrated load effect but also the fact that masonry have relatively small flexural tensile strength, but not zero, as is usually considered in the theoretically behavior.

In both, the dimensional and nondimensional N–M interaction diagrams, the four straight lines that indicate the studied eccentricities pass through the points of the theoretical curves and through the points of the experimental curves for those same eccentricities and all these points are aligned with the origin.

A discontinuity is observed in the experimental N–M curves for the eccentricity  $e_2 = t/4 = 0.25 \cdot t = 70$  mm with respect to the theoretical curve. This slight discontinuity produces a drop in strength that may be caused by a possible defect in the construction or geometry of the elements.

## 6 | DESIGN RECOMMENDATIONS

In this section, the mechanical behavior of the arch shown in Figure 2 and created with the voussoirs studied in this research (Figure 1) is analytically studied. Firstly, the greatest internal forces that arch will experience are calculated, considering applied loads according to current design regulations. Next, these maximum internal forces will be compared with the experimental nondimensional N–M interaction diagram (Figure 13) to check if the arch is capable of bearing the applied loads. Finally, the geometry of the arch and the applied loads will be varied to offer design recommendations. The objective of this study is to check at a sectional level if the arch shown in Figure 2 is capable of bearing the applied design loads. The analysis of instability and possible local problems is outside the scope of this study, which should be verified in future investigations with experimental tests of arches.

Four types of boundary conditions were studied: (1) both supports encastred, (2) one support encastred and the other with all the degrees of freedom (DOFs) fixed except horizontal displacement, (3) both supports pinned, and (4) one support pinned and the other with all the translational DOFs fixed except horizontal displacement (isostatic arch). Configuration (1) corresponds to that shown in Figure 2. Configuration (2) is studied in the case of a horizontal displacement of one of the

supports of the previous configuration occurs. Configuration (3) is studied in case the fixity of rotational DOF fails and (4) is studied in case, in addition, the horizontal displacement of a support occurs.

### 6.1 | Applied loads

The considered applied loads are in accordance with the CTE.<sup>37</sup> The permanent loads are the self-weight of the arch and the weight of a 30 cm thick slab supported by the arch. The specific weight considered for the masonry of the arch and for the slab is 23 kN/m<sup>3</sup>. The considered uniformly distributed imposed load is 1 kN/m<sup>2</sup> and a mobile point load of 2 kN, not acting simultaneously. These imposed loads correspond to passable roofs. The tributary width is 5 m, that is, the arches are separated 5 m each other. The partial safety factors are 1.35 for permanent loads and 1.5 for variable loads. Taking into account all these considerations, the design load of the permanent loads is  $G_d = 49.1$  kN/m, the design value of the uniformly distributed imposed load is  $Q_{dd} = 5$  kN/m and the design value of point load is  $Q_{pd} = 3$  kN.

The analyzed loading hypotheses are four: hypothesis of maximum and minimum bending moments, with their associated concomitant axial loads and the hypothesis of maximum and minimum axial loads, with their associated concomitant bending moments. The uniformly distributed imposed load acts on the fraction of the arch that generates the worst internal forces for each loading hypothesis, as occurs with the point load.

### 6.2 | Internal forces

The fundamental hypothesis is that the arch curvature is small compared to the transverse dimensions of their section, or what is the same, that the radius of curvature is much greater than the section height. This simplification is normally applicable if the ratio of the radius of curvature to the height is greater than 10,<sup>38</sup> which is the case of the studied arch. The assumption of small curvature means that it is not necessary to apply a special theory of curved parts, but the conventional theory of bending of beams is directly applicable, considering only that the domain of the structure is curved. Other adopted hypotheses are: (1) neglecting shear energy since, by their own definition, arcs are slender, so the shear energy is not significant,<sup>38</sup> (2) neglecting the axial stress energy.<sup>38</sup>

Axes located in the keystone of the arch are adopted (Figure 14). The expression of its directrix referred to these axes is shown in Equation (3).

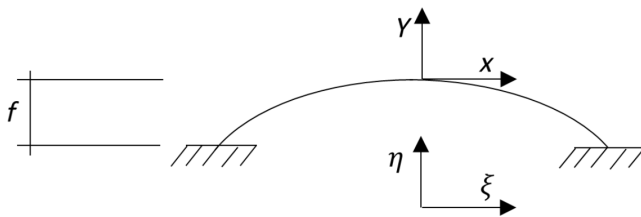


FIGURE 14 Coordinate axes

$$y = \sqrt{R^2 - x^2} - R \quad (3)$$

On the other hand, the differential arch length follows the Equation (4)

$$\begin{aligned} ds &= \sqrt{dx^2 + dy^2} = \sqrt{1 + \left(\frac{dy}{dx}\right)^2} dx \\ &= \sqrt{1 + \left(-\frac{x}{\sqrt{R^2 - x^2}}\right)^2} dx \end{aligned} \quad (4)$$

where:

$$\frac{dy}{dx} = -\frac{x}{\sqrt{R^2 - x^2}} \quad (5)$$

Hereafter a distinction is made between the encastred and pinned arch in analytical procedure.

### 6.2.1 | Encastred arch

As the arch is symmetrical, the elastic center is on its symmetry axis. The vertical coordinate of the elastic center  $y_E$  is calculated using the Equation (6).

$$y_E = \frac{\int y/EI ds}{\int 1/EI ds} \quad (6)$$

where:  $EI$ , Bending stiffness of the section.  $E$  is the elasticity modulus and  $I$  is the inertia moment of the arch section.

A new coordinate axis  $(\xi, \eta)$ , which are located at the elastic center and are parallel to the original ones  $(x, y)$  are defined (Figure 14). The relationship between the coordinates in both systems is shown in Expressions (7) and (8).

$$\xi = x \quad (7)$$

$$\eta = y - y_E \quad (8)$$

Next, the arch analysis is carried out taking as hyperstatic unknowns the three reactions in the left encastred support (force in direction  $\xi$  ( $F_\xi$ ), force in direction  $\eta$  ( $F_\eta$ ) and the bending moment ( $M_E$ )). Imposing unit values of  $F_\xi$ ,  $F_\eta$ , and  $M_E$ , and using the corresponding compatibility equations, the matrix Equation (9) is obtained where the only unknowns are  $F_\xi$ ,  $F_\eta$ , and  $M_E$ .<sup>38</sup> The fact of using the elastic center as the reference coordinate system causes the hyperstatic unknowns to be uncoupled. The force  $F_\xi$  would become zero when the horizontal displacement of one support was allowed.

$$\begin{bmatrix} I_{02}^e & 0 & 0 \\ 0 & I_{20}^e & 0 \\ 0 & 0 & I_{00} \end{bmatrix} \begin{pmatrix} F_\xi \\ F_\eta \\ M_E \end{pmatrix} = \begin{pmatrix} \int M^0_{\eta/EI} ds \\ -\int M^0_{\xi/EI} ds \\ \int M^0_{/EI} ds \end{pmatrix} \quad (9)$$

where:

$$I_{00} = \int 1/EI ds \quad (10)$$

$$I_{20}^e = \int \xi^2/EI ds \quad (11)$$

$$I_{02}^e = \int \eta^2/EI ds \quad (12)$$

$M^0$ , bending moment in each arch section in the isostatic case (Figure 15).

Once the values of  $F_\xi$ ,  $F_\eta$ , and  $M_E$  are known, the value of the bending moment for any section of the arch is given by Equation (13).

$$M = M^0 - F_\xi \eta + F_\eta x - M_E \quad (13)$$

The value of the internal axial load for any section of the arch is given by Equation (14).

$$N = N^0 - F_\xi \cos(\alpha) - F_\eta \sin(\alpha) \quad (14)$$

where  $N^0$ , internal axial load in each arch section in the isostatic case (Figure 15).

### 6.2.2 | Pinned-pinned arch

In this case, it is not necessary to use the elastic center. The arch analysis is performed taking as the hyperstatic unknown

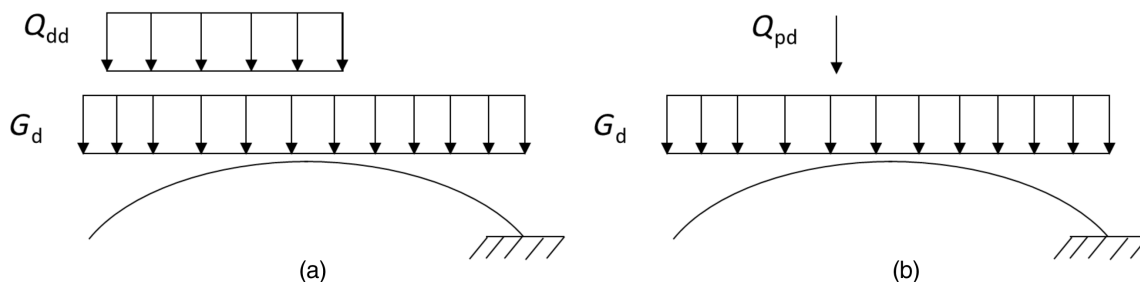
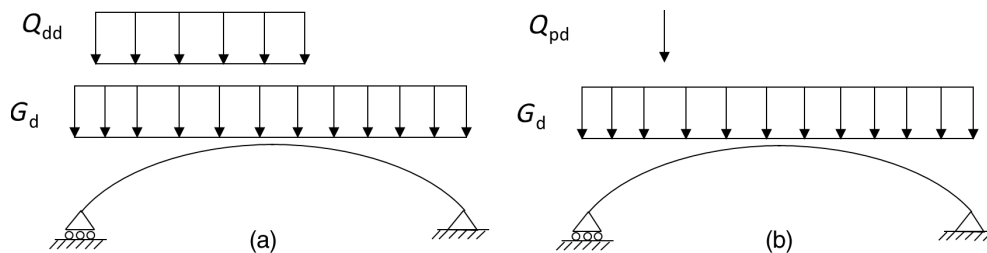


FIGURE 15 Permanent load and distributed imposed load on the cantilever isostatic arch: (a) uniformly distributed imposed load, (b) point imposed load

FIGURE 16 Permanent load and distributed imposed load on the pinned isostatic arch: (a) uniformly distributed imposed load, (b) point imposed load



the horizontal reaction in the left support ( $A_x$ ). The expression for  $A_x$  is obtained by imposing a unit value of said reaction and using the corresponding compatibility equations (Equation 15).<sup>38</sup> The force  $A_x$  would become zero when the horizontal displacement of one support was allowed.

$$A_x = \frac{\int M^0/EI \cdot (y+f) ds}{\int (y+f)^2 ds} \quad (15)$$

where  $f$ , Arch height (Figure 14).  $M^0$ , bending moment in each arch section in the isostatic case (Figure 16).

Once the value  $A_x$  is known, the value of the bending moment for any section of the arch is given by the Equation (16).

$$M = M^0 - A_x(y+f) \quad (16)$$

The value of the internal axial load for any section of the arch is given by the Equation (17).

$$N = N^0 - A_x \cos(\alpha) \quad (17)$$

where:  $N^0$ , axial load in each arch section in the isostatic case (Figure 16).

### 6.3 | Results

Table 5 shows the most unfavorable internal forces in the arch after performing the analysis. These results are computed considering the applied loads shown in Section 6.1

for the four load hypotheses considered: hypothesis of maximum and minimum bending moments, with their associated concomitant axial forces and hypothesis of maximum and minimum axial loads, with their concomitant bending moments. The results shown in Table 5 correspond to those originated due to uniformly distributed imposed load. The point-imposed load causes much lower internal forces and those results are omitted. According to the CTE<sup>37</sup> the uniformly distributed load and the point load should not be considered acting simultaneously.

If the nondimensional values of the internal forces in Table 5 are compared with the more conservative curve of the nondimensional N–M interaction diagram of Figure 13, which is the theoretical curve that does not take into account the effect of the concentrated load, it can be concluded that the arch can resist the applied loads to which it is subjected. If the applied load is increased until the failure, the arch can bear an additional distributed load of 1.8 kN/m<sup>2</sup>. This additional strength capacity can be used to bear snow or wind loads, depending on the geographic location of the arch.

Table 5 does not show the results when horizontal displacement of a support is allowed (either in the pinned or encastred case) because the internal bending moments are very high and exceed the strength capacity of the arch. Therefore, the design of the arch must assure that the supports do not undergo horizontal displacements by means of steel ties between the supports or any other mechanical mechanism.

The analysis was also carried out for different arch lengths  $L$  (from  $L = 4$  to 9 m) and for different tributary widths the arch (from 2 to 8 m), keeping the radius at 6 m, as indicated in Figure 2. The results obtained were the maximum distributed load extended in the region that causes

TABLE 5 Most unfavorable internal forces in the arch

Boundary conditions	Load hypothesis of max. and min. bending moment				Max. absolute values		Nondimensional values	
	$M_{\max}$	$N_{\text{concomitant}}$	$M_{\min}$	$N_{\text{concomitant}}$	$M$	$N_{\text{concomitant}}$	$M$	$N_{\text{concomitant}}$
Encastred-encastred	8.49	-343.19	-3.66	-319.94	8.49	343.19	0.42	0.59
Pinned-pinned	4.36	-300.88	-7.00	-318.91	7.00	318.91	0.35	0.55
	Load hypothesis of max. and min. axial load				$N$	$M_{\text{concomitant}}$	$N$	$M_{\text{concomitant}}$
	$N_{\max}$	$M_{\text{concomitant}}$	$N_{\min}$	$M_{\text{concomitant}}$				
Encastred-encastred	-307.14	2.33	-349.79	1.05	349.79	1.05	0.61	0.05
Pinned-pinned	-299.69	3.62	-342.73	0.00	342.73	0.00	0.59	0.00

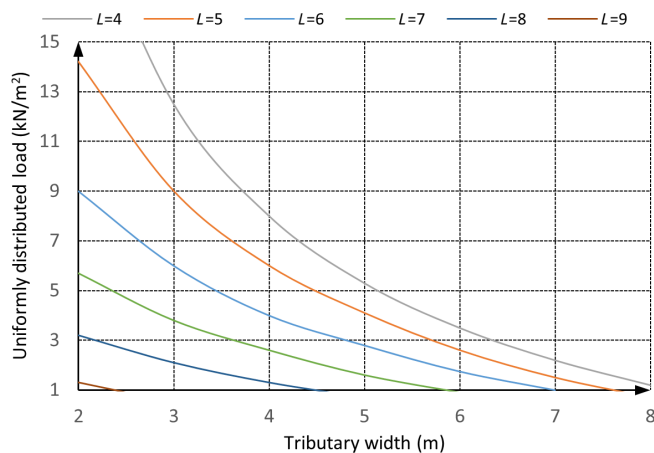


FIGURE 17 Maximum allowable imposed distributed load for a tributary width and arch length

the worst internal forces that the arch can withstand, that is, the internal forces that are in the limit of the theoretical line in the N–M interaction diagram (Figure 13). These results are shown in Figure 17. The lower limit the load is  $1 \text{ kN/m}^2$ , which corresponds to the uniformly distributed imposed load for roofs according to the CTE.<sup>37</sup> The rest of the loading capacity can be used to bear snow loads or certain other actions depending on where the structure will be located. Therefore, the arch maximum length can be obtained for a given tributary width and distributed applied load by using Figure 16. For usual tributary widths of 5 or 6 m the maximum arch lengths would be 7 or 6 m, respectively. Arch lengths beyond 8 m are not appropriate because the associated tributary width is very small and would require many parallel arches to bear the roof.

## 7 | CONCLUSIONS

An experimental study of masonry specimens made with special voussoirs subjected to centered compression, eccentric compression and simple bending has been carried out. Subsequently, an analytical study of an arch made with these voussoirs was performed. The following

conclusions can be drawn from the results of the present research:

- When the masonry specimens are tested under eccentric compression, an increase in the ultimate axial stress  $\sigma_k$  is observed with respect to ultimate axial stress in pure compression  $\sigma_{k0}$  because of the concentrated load effect, which varies from 1225 for small eccentricities up to 2236 for large eccentricities.
- This type of masonry, according to the obtained results, develops an ultimate bending moment  $M_u$  under simple bending with a value equal to  $0.234 \cdot M_p$ ; where  $M_p$  is the plastic bending moment of the section whose value is  $M_p = (b \cdot t^2 \cdot \sigma_{k0})/8$ . The ultimate bending moment stress  $\sigma_{xk}$  ( $\sigma_{xk} = M_u/W_y$ , where  $W_y$  is the elastic section modulus) of this type of masonry is 17% of the ultimate compressive stress under pure compression,  $\sigma_{xk} = 0.17 \cdot \sigma_{k0}$ .
- If an extrapolation of the N–M diagrams is performed, the pure tensile strength of the masonry can be computed  $0.086 \cdot N_p$ , where  $N_p$  is the plastic axial load of the section  $N_p = b \cdot t \cdot \sigma_{k0}$ . This implies that the masonry pure tensile strength is of the order of 10% of the ultimate axial stress:  $\sigma_{tk} = 0.10 \cdot \sigma_{k0}$ . This ratio is greater than that found in the scientific literature by other authors,<sup>29–35</sup> due to the fact that the mortar used in this experimental research had greater strength than is commonly used in masonry construction. The special geometry of the voussoirs can also influence this fact. Moreover, the qualification of the workmanship is a factor that can influence the dispersion of the masonry strength.
- The real masonry strength under both simple bending and eccentric compression, is much higher than the expected theoretical strength. The reason is basically the concentrated load effect but also the fact that masonry have relatively small flexural tensile strength, but not zero, as is usually considered in their theoretically behavior.
- Comparison between the nondimensional values of the internal forces in the arch obtained from the analytical study, and the interaction N–M diagram

obtained experimentally, shows that the arch is capable of bearing the design regulations actions for a wide range of arch lengths and distributed applied load values. This is valid for both encastred and pinned arches.

- The supports of the arch cannot undergo horizontal displacements because the internal bending moments that the arch would suffer would exceed its strength capacity.
- The maximum arch lengths are 7 or 6 m for usual tributary widths of 5 or 6 m respectively. Arch lengths beyond 8 m are not appropriate because the associated tributary width is very small and would require many parallel arches to bear the roof.

## ACKNOWLEDGMENT

The authors would like to acknowledge the help of Estefanía Soler, graduate student in Architectural technology from University of Alicante.

## DATA AVAILABILITY STATEMENT

The data that support the findings of this study are available from the corresponding author upon reasonable request.

## ORCID

Juan Carlos Pomares Torres  <https://orcid.org/0000-0002-6773-9112>

Javier Pereiro-Barceló  <https://orcid.org/0000-0002-4164-0050>

## REFERENCES

- Manterola J. Evolución de los puentes en la historia reciente. *Inf Constr.* 1984;35:5–35. <https://doi.org/10.3989/ic.1984.v35.i359-360.1949>
- Lahuerta JA. Cálculo de la fábrica armada. In *Constr.* 1992;44:71–93. <https://doi.org/10.3989/ic.1992.v44.i421.1315>
- Grimm CT. Void mortar joints: bane of brick masonry. *J Constr Eng Manag.* 1994;120:152–61. [https://doi.org/10.1061/\(ASCE\)0733-9364\(1994\)120:1\(152\)](https://doi.org/10.1061/(ASCE)0733-9364(1994)120:1(152))
- Doherty K, Griffith MC, Lam N, Wilson J. Displacement-based seismic analysis for out-of-plane bending of unreinforced masonry walls. *Earthq Eng Struct Dyn.* 2002;31:833–50. <https://doi.org/10.1002/eqe.126>
- Santiago HF. Arcos bóvedas y cúpulas. Geometría y equilibrio en el cálculo tradicional de estructuras de fábrica. Madrid: Instituto Juan de Herrera; 2004.
- Gilbert M. Limit analysis applied to masonry arch bridges: state-of-the-art and recent developments. 5th International Conference on Arch Bridges, Madeira; 2007; pp. 13–28.
- Carbonell A, Yepes V, González-Vidosa F. Búsqueda exhaustiva por entornos aplicada al diseño económico de bóvedas de hormigón armado. *Rev Int Metodos Numer para Calc Diseno Ing.* 2011;27:227–35. <https://doi.org/10.1016/j.rimni.2011.07.003>
- García Sanz Calcedo J, Fortea Luna M, Reyes Rodríguez AM. Análisis comparativo en base a la sostenibilidad ambiental entre bóvedas de albañilería y estructuras de hormigón. *Rev Ing Constr.* 2012;27:5–22. <https://doi.org/10.4067/s0718-50732012000100001>
- Coccia S, Di Carlo F, Rinaldi Z. Collapse displacements for a mechanism of spreading-induced supports in a masonry arch. *Int J Adv Struct Eng.* 2015;7:307–20. <https://doi.org/10.1007/s40091-015-0101-x>
- Trias de Bes J, Casariego P. De la técnica a la tecnología: Construcción de forjados de cerámica abovedada mediante sistemas industrializados. *Inf La Constr.* 2016;68:17–8. <https://doi.org/10.3989/ic.15.168.m15>
- Urruchi-Rojo JR, Martínez-Martínez JA, Serrano-López R. De la bóveda de medio punto a la bóveda escarzana en los puentes de piedra. Influencia del rebajamiento y del relleno rígido en la variación de la carga de rotura. *Inf La Constr.* 2017;69:e187. <https://doi.org/10.3989/ic.15.107>
- Portioli F, Cascini L. Large displacement analysis of dry-jointed masonry structures subjected to settlements using rigid block modelling. *Eng Struct.* 2017;148:485–96. <https://doi.org/10.1016/j.engstruct.2017.06.073>
- Thaickavil NN, Thomas J. Behaviour and strength assessment of masonry prisms. *Case Stud Constr Mater.* 2018;8:23–38. <https://doi.org/10.1016/j.cscm.2017.12.007>
- Hernando García JI, Magdalena Layos F, Aznar LA. Cracking of masonry arches with great deformations: a new equilibrium approach. *J Mech Mater Struct.* 2018;13:647–56. <https://doi.org/10.2140/jomms.2018.13.647>
- Galassi S, Misseri G, Rovero L, Tempesta G. Failure modes prediction of masonry voussoir arches on moving supports. *Eng Struct.* 2018;173:706–17. <https://doi.org/10.1016/j.engstruct.2018.07.015>
- Pomares JC, González A, Saura P. Simple and resistant construction built with concrete Voussoirs for developing countries. *J Constr Eng Manag.* 2018;144(10):04018076-1–10. [https://doi.org/10.1061/\(ASCE\)JC0.1943-7862.0001532](https://doi.org/10.1061/(ASCE)JC0.1943-7862.0001532)
- Abdulhameed AA, Said AMI. Experimental investigation of the behavior of self-form segmental concrete masonry arches. *Fibers.* 2019;7:58. <https://doi.org/10.3390/FIB7070058>
- Bautista A, Pomares JC, González MN, Velasco F. Influence of the microstructure of TMT reinforcing bars on their corrosion behavior in concrete with chlorides. *Construct Build Mater.* 2019;229:116899. <https://doi.org/10.1016/J.CONBUILDMAT.2019.116899>
- Pavlu T, Fortova K, Divis J, Hajek P. The utilization of recycled masonry aggregate and recycled EPS for concrete blocks for mortarless masonry. *Materials (Basel).* 2019;12:1923. <https://doi.org/10.3390/ma12121923>
- Tempesta G, Galassi S. Safety evaluation of masonry arches. A numerical procedure based on the thrust line closest to the geometrical axis. *Int J Mech Sci.* 2019;155:206–21. <https://doi.org/10.1016/j.ijmecsci.2019.02.036>
- Coccia S, Di Carlo F. Collapse of elliptical masonry arch induced by actual displacements of the supports. International conference of numerical analysis and applied mathematics ICNAAM 2019; 2020; Vol. 2293, p. 240012. <https://doi.org/10.1063/5.0026466>
- Adell JM, Rolando A. Luis Moya y las bóvedas tabicadas en la posguerra española. *Inf Constr.* 2005;56:25–9. <https://doi.org/10.3989/ic.2005.v57.i496.460>
- García-Gutiérrez Mosteiro J. Las bóvedas tabicadas de Guastavino: forma y construcción. *Actas del Tercer Congreso Nacional de Historia de la Construcción.* Sevilla: Instituto Juan de Herrera; 2000. p. 365–74.
- Fomento M. Instrucción de Hormigón Estructural (EHE-08). 2008.
- Asociación española de normalización. UNE-EN 1015-11 Métodos de ensayo de los morteros para albañilería. Parte 11:



Determinación de la resistencia a flexión y a compresión del mortero endurecido. Spain; 2000.

26. De Fomento M. Seguridad estructural. Spain: Fábrica; 2019.
27. De Fomento M. Instrucción para la recepción de cementos RC-16: con comentarios de los miembros de la Comisión Permanente del Cemento. Spain; 2018.
28. UNE-EN 1052-1 Método de ensayo para fábricas de albañilería. Parte 1: Determinación de la resistencia a compresión. Spain; 1999.
29. Abdulla KF, Cunningham LS, Gillie M. Simulating masonry wall behaviour using a simplified micro-model approach. *Eng Struct*. 2017;151:349–65. <https://doi.org/10.1016/j.engstruct.2017.08.021>
30. Milani G, Lourenço P, Tralli A. Homogenization approach for the limit analysis of out-of-plane loaded masonry walls. *J Struct Eng*. 2006;132:1650–63. [https://doi.org/10.1061/\(asce\)0733-9445\(2006\)132:10\(1650\)](https://doi.org/10.1061/(asce)0733-9445(2006)132:10(1650))
31. Lourenço PB, Barros J, Almeida JC. Characterization of masonry under uniaxial tension. VII. Int. Semin Struct Mason Dev Ctries; 2002; p. 24.
32. Maheri MR, Motielahi F, Najafgholipour MA. The effects of pre and post construction moisture condition on the in-plane and out-of-plane strengths of brick walls. *Mater Struct Constr*. 2011;44:541–59. <https://doi.org/10.1617/s11527-010-9648-y>
33. Hetherington S, Hetherington S. A comparative study into the tensile bond strength of the brick mortar interface of naturally hydraulic lime and Portland cement mortars. *Mason Int*. 2015;28:64–7.
34. Pavia S, Hanley R. Flexural bond strength of natural hydraulic lime mortar and clay brick. *Mater Struct*. 2010;43:913–22. <https://doi.org/10.1617/s11527-009-9555-2>
35. European Comission. Eurocode 6: Design of masonry structures. Part 1-1: General rules for reinforced and unreinforced masonry structures. UNE-EN 1996- 1-1:2011+A1.
36. Lacidogna G, Accornero F. Elastic, plastic, fracture analysis of masonry arches: a multi-span bridge case study. *Curved Layer Struct*. 2018;5:1–9. <https://doi.org/10.1515/cls-2018-0001>
37. de Fomento M. Documento básico SE-AE Seguridad Estructural. Acciones en la Edificación. Código Técnico La Edif; 2009; 1–42.
38. Celigüeta Lizarza JT. Curso de análisis estructural. Navarra; 2003.

## AUTHOR BIOGRAPHIES



**Juan Carlos Pomares Torres**, Associate Professor, Department of Civil Engineering, University of Alicante, PO Box 99, Alicante 03690, Spain. Email: jc.pomares@ua.es



**Antonio González Sánchez**, Associate Professor, Department of Civil Engineering, University of Alicante, PO Box 99, Alicante 03690, Spain. Email: antonio.gonzalez@ua.es



**Javier Pereiro Barceló**, Assistant Professor, Department of Civil Engineering, University of Alicante, PO Box 99, Alicante 03690, Spain. Email: javier.pereiro@ua.es



**Pascual Saura Gómez**, Assistant Professor, Department of Architectural Constructions, University of Alicante, PO Box 99, Alicante 03690, Spain. Email: pascual.saura@ua.es



**Benjamín Torres Górriz**, Head of Laboratory, Department of Civil Engineering, University of Alicante, PO Box 99, Alicante 03690, Spain. Email: benjamin.torres@ua.es

**How to cite this article:** Pomares Torres JC, González Sánchez A, Pereiro-Barceló J, Saura Gómez P, Torres B. Strength capacity of prismatic specimens for masonry constructions made of concrete voussoirs. *Structural Concrete*. 2022;23: 2878–94. <https://doi.org/10.1002/suco.202100573>